CHEMISTRY OF MATERIALS

ARTICLE

pubs.acs.org/cm

Structure and Magnetic Properties of $BiFe_{0.75}Mn_{0.25}O_3$ Perovskite Prepared at Ambient and High Pressure

Alexei A. Belik,*[,†] Artem M. Abakumov,[‡] Alexander A. Tsirlin,[§] Joke Hadermann,[‡] Jungeun Kim,[∥] Gustaaf Van Tendeloo,[‡] and Eiji Takayama-Muromachi[⊥]

[†]International Center for Materials Nanoarchitectonics (MANA), National Institute for Materials Science (NIMS), 1-1 Namiki, Tsukuba, Ibaraki 305-0044, Japan

[‡]Electron Microscopy for Materials Science (EMAT), University of Antwerp, Groenenborgerlaan 171, B-2020 Antwerp, Belgium

[§]Max Planck Institute for Chemical Physics of Solids (MPI CPfS), Nöthnitzer Strasse 40, 01187 Dresden, Germany

[∥]Japan Synchrotron Radiation Research Institute (JASRI), 1-1-1 Kouto, Sayo-cho, Hyogo 679-5198, Japan

[⊥]National Institute for Materials Science (NIMS), 1-2-1 Sengen, Tsukuba, Ibaraki 305-0047, Japan

Supporting Information

ABSTRACT: Solid solutions of $BiFe_{1-x}Mn_xO_3$ ($0.0 \le x \le 0.4$) were prepared at ambient pressure and at 6 GPa. The ambient-pressure (AP) phases crystallize in space group $R3c$ similarly to $BiFeO_3$. The high-pressure (HP) phases crystallize in space group $R3c$ for $x = 0.05$ and in space group $Pnma$ for $0.15 \le x \le 0.4$. The structure of HP-$BiFe_{0.75}Mn_{0.25}O_3$ was investigated using synchrotron X-ray powder diffraction, electron diffraction, and transmission electron microscopy. HP-$BiFe_{0.75}Mn_{0.25}O_3$ has a $PbZrO_3$-related $\sqrt{2}a_p \times 4a_p \times 2\sqrt{2}a_p$ (a_p is the parameter of the cubic perovskite subcell) superstructure with $a = 5.60125(9)$ Å, $b = 15.6610(2)$ Å, and $c = 11.2515(2)$ Å similar to that of $Bi_{0.82}La_{0.18}FeO_3$. A remarkable feature of this structure is the unconventional octahedral tilt system, with the primary $a^-b^0a^-$ tilt superimposed on pairwise clockwise and counterclockwise rotations around the b-axis according to the $oioi$ sequence (o stands for out-of-phase tilt, and i stands for in-phase tilt). The $(FeMn)O_6$ octahedra are distorted, with one longer metal−oxygen bond (2.22−2.23 Å) that can be attributed to a compensation for covalent Bi−O bonding. Such bonding results in the localization of the lone electron pair on Bi^{3+} cations, as confirmed by electron localization function analysis. The relationship between HP-$BiFe_{0.75}Mn_{0.25}O_3$ and antiferroelectric structures of $PbZrO_3$ and $NaNbO_3$ is discussed. On heating in air, HP-$BiFe_{0.75}Mn_{0.25}O_3$ irreversibly transforms to AP-$BiFe_{0.75}Mn_{0.25}O_3$ starting from about 600 K. Both AP and HP phases undergo an antiferromagnetic ordering at $T_N \approx 485$ and 520 K, respectively, and develop a weak net magnetic moment at low temperatures. Additionally, ceramic samples of AP-$BiFe_{0.75}Mn_{0.25}O_3$ show a peculiar phenomenon of magnetization reversal.

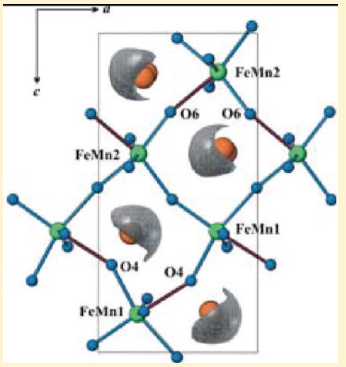

KEYWORDS: $BiFeO_3$, multiferroics, high pressure, superstructure

1. INTRODUCTION

$BiFeO_3$ is a perovskite-type oxide crystallizing in space group $R3c$ with $a = 5.579$ Å and $c = 13.869$ Å (in a hexagonal setting) at room temperature (RT) and ambient pressure (AP). $BiFeO_3$ is both ferroelectric (with a ferroelectric Curie temperature, T_E, of 1100 K) and antiferromagnetic (with Néel temperature, T_N, of 640 K).[1,2] Materials of this kind are termed multiferroics. In multiferroic systems, two or all three of the properties (anti)-ferroelectricity, (anti)ferromagnetism, and ferroelasticity are observed simultaneously.[3] The spins are canted in $BiFeO_3$ below T_N. However, due to the cycloidal rotation of the canted antiferromagnetic spins, the net moment is zero, and $BiFeO_3$ is a pure antiferromagnet.[1]

Chemical substitutions have been widely explored in an effort to induce the net magnetization in $BiFeO_3$, reduce the current leakage, improve the switchable ferroelectric behavior, and enhance the magnetoelectric coupling.[4,5] Regarding the magnetism, doping on the A-site should lead to moderate changes in the system, whereas doping on the B-site directly affects magnetic couplings. This fact stimulated several attempts to prepare $BiFe_{1-x}Mn_xO_3$ solid solutions,[6−12] where Mn^{3+} is chosen due to its similar size but different electronic structure and tendency toward ferromagnetic couplings (the end member $BiMnO_3$ is an orbitally ordered ferromagnetic insulator).[13]

At AP, the solubility range of manganese in $BiFeO_3$ is limited by $x \le 0.3$ and accompanied by a marginal excess of oxygen, with $\delta = 0.015−0.06$ for $BiFe_{1-x}Mn_xO_{3+\delta}$.[10] The rhombohedral $R3c$ structure of $BiFeO_3$ is maintained up to the solubility limit.[6,10,11]

Compared to the sample preparation at AP, the high-pressure (HP) synthetic method has several advantages, in particular (i) solid solution or dopant solubility ranges can be expanded, (ii) high-density ceramics required for dielectric measurements are obtained, (iii) the oxygen content is maintained, and

Received: June 22, 2011
Revised: September 1, 2011
Published: September 29, 2011

(iv) novel structural modifications can be stabilized. Experimental works on the HP preparation of $BiFeO_3$-based solid solutions are, nevertheless, rather scarce.[8,12,14−17] In the $BiFe_{1-x}Mn_xO_3$ system, the HP synthesis gives access to the whole compositional range and, specifically, to a novel orthorhombic $PbZrO_3$-type phase at $0.2 \leq x \leq 0.6$.[8,12] The complete structure solution for this phase has not been reported, although a recent work[12] claims the possible ordering of Fe^{3+} and Mn^{3+} cations and an unusual magnetization reversal behavior at $x = 0.5$.

In this study, we combine high-resolution synchrotron X-ray diffraction and electron microscopy techniques to study the crystal structure of the HP-$BiFe_{1-x}Mn_xO_3$ phase at $x = 0.25$. We also report the magnetic properties of this phase and compare them to the data for the AP-$BiFe_{1-x}Mn_xO_3$ and parent $BiFeO_3$ compounds.

2. EXPERIMENTAL SECTION

2.1. Synthesis of $BiFe_{1-x}Mn_xO_3$. Samples with x = 0.05, 0.1, 0.15, 0.2, 0.25, 0.3, and 0.4 were synthesized from stoichiometric mixtures of Bi_2O_3 (99.9999%), Fe_2O_3 (99.999%), and Mn_2O_3 (99.99%). For the AP synthesis ($0.05 \leq x \leq 0.25$), mixed powders were pressed into pellets and annealed at 1143 K for 2 h on Pt plates with subsequent quenching in air. One pellet of each composition was used to prevent the direct contact between the Pt plate and the remaining part of the sample because of a possible reaction between Pt and Bi_2O_3.[1] The heating time to 1143 K was 2 h. AP-$BiFe_{1-x}Mn_xO_3$ contained a trace amount of $Bi_{25}(Fe,Mn)O_{39+\delta}$ as an impurity (see the Supporting Information).

The HP phases ($0.05 \leq x \leq 0.40$) were prepared from the same starting mixtures of oxides in a belt-type high-pressure apparatus at 6 GPa and 1400 K for 90 min in sealed Au capsules. After heat treatment, the samples were quenched to RT, and the pressure was slowly released. Treatment of AP-$BiFe_{0.75}Mn_{0.25}O_3$ at the same synthesis conditions transforms it to HP-$BiFe_{0.75}Mn_{0.25}O_3$ (see the Supporting Information). This experiment was performed to check that a possible variation in the oxygen content is not responsible for different crystal structures.

2.2. Characterization of $BiFe_{1-x}Mn_xO_3$. X-ray powder diffraction (XRD) data were collected at RT on a RIGAKU Ultima III diffractometer using Cu Kα radiation (2θ range of 5−100°, a step width of 0.02°, and a counting time of 2−10 s/step). RT and high-temperature (HT) synchrotron XRD data were collected on a large Debye−Scherrer camera at the BL02B2 beamline[18] of SPring-8 from 290 to 950 K. HT synchrotron XRD data were collected for 5 min at each temperature with a heating time of 1−2 min between adjacent temperatures. The incident beam from a bending magnet was monochromatized to λ = 0.41916 Å. The samples were contained in (boro)glass and quartz capillary tubes with an inner diameter of 0.2 mm, and the capillary tubes were spun during the measurements. The synchrotron XRD data were collected in a 2θ range from 2° to 75° with a step of 0.01° (the data from 2° to 52° were used in the refinements). Diffraction data were analyzed by the Rietveld method with the JANA2006 program.[19]

The oxygen content of AP-$BiFe_{0.75}Mn_{0.25}O_{3+\delta}$ and HP-$BiFe_{0.75}Mn_{0.25}O_{3+\delta}$ is $\delta = -0.01(1)$ and 0.02(1), respectively, as determined by thermogravimetric analysis (TGA). The samples were placed into Al_2O_3 crucibles, heated in 5 h to 873 K, soaked for 3 h at 873 K in 100% H_2, and cooled to RT in a flow of 100% H_2. The experiment was performed in a tube furnace. The sample weights were measured before and right after the reduction. All samples were reduced in one experiment.

Magnetization measurements were performed on a SQUID magnetometer (Quantum Design, MPMS) between 2 and 400 K (and between 300 and 750 K) in applied fields of 100 Oe, 10 kOe, and 50 kOe under both zero-field-cooled (ZFC) and field-cooled (FC; on cooling) conditions using pellets of $BiFeO_3$ and AP-$BiFe_{0.75}Mn_{0.25}O_3$ and a powder of HP-$BiFe_{0.75}Mn_{0.25}O_3$. Isothermal magnetization measurements were performed from +50 to −50 kOe and from −50 to +50 kOe at 5 and 300 K (500 and 600 K for $BiFeO_3$). Specific heat (C_p) measurements were performed at a zero magnetic field on cooling from 300 to 2 K by a pulse relaxation method using a commercial calorimeter (Quantum Design, PPMS). AP-$BiFe_{0.75}Mn_{0.25}O_3$ and HP-$BiFe_{0.75}Mn_{0.25}O_3$ showed almost identical C_p versus T curves (see the Supporting Information).

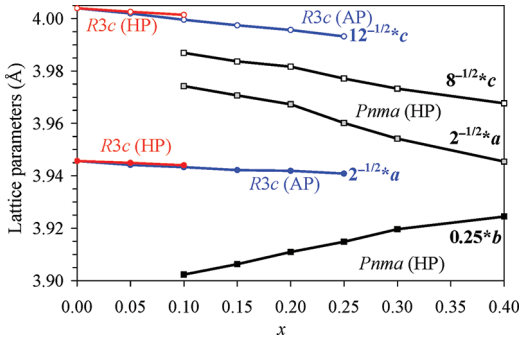

Figure 1. Compositional dependence of the lattice parameters in AP-$BiFe_{1-x}Mn_xO_3$ for $0.0 \leq x \leq 0.25$ (space group $R3c$), HP-$BiFe_{1-x}Mn_xO_3$ for $0.0 \leq x \leq 0.10$ (space group $R3c$), and HP-$BiFe_{1-x}Mn_xO_3$ for $0.10 \leq x \leq 0.40$ (space group $Pnma$). The lattice parameters are normalized to the parameter of the cubic perovskite subcell (a_p).

Differential scanning calorimetry (DSC) curves were recorded on a Mettler Toledo DSC1 STAR^e system at a heating/cooling rate of 10 K/min under N_2 flow from 293 to 570−870 K in open Pt capsules. DSC measurements were cycled between 293 and 570 K several times to check the reproducibility of thermal effects.

A sample for transmission electron microscopy (TEM) was prepared by crushing the material in an agate mortar under ethanol and depositing it on holey carbon grids. Electron diffraction (ED) patterns were obtained with a Philips CM20 microscope. High-resolution high-angle annular dark field scanning TEM (HAADF-STEM) images, annular bright field STEM (ABF-STEM) images, and energy-dispersive X-ray (EDX) spectra were obtained using a Titan G3 electron microscope operated at 300 kV and equipped with an aberration probe corrector and EDAX analyzer. HAADF-STEM and ABF-STEM image simulations were made using the QSTEM software.[20]

The electron localization function (ELF) was computed from the charge density obtained in self-consistent band-structure calculations based on density functional theory (DFT). We used the TB-LMTO-ASA code[21] with the exchange-correlation potential by Perdew and Wang.[22] The symmetry-irreducible part of the first Brillouin zone was sampled with 105 k-points. Experimental atomic positions for HP-$BiFe_{0.75}Mn_{0.25}O_3$ were taken as an input. The cation disorder was eliminated by occupying the mixed FeMn positions with Fe or Mn exclusively. Basic features of the ELF for the resulting (fictitious) $BiFeO_3$ and $BiMnO_3$ compounds essentially matched. Calculated energy spectra are typical for Bi-containing transition-metal compounds treated in local density approximation[23] and comprise Bi 6s states below −10 eV, O 2p states between −8 and −2 eV, and Fe/Mn 3d states in the vicinity of the Fermi level.

3. RESULTS

3.1. Ambient-Pressure Phases. In agreement with the previous studies,[6,9−11] the AP phases crystallize in the space group $R3c$. The compositional dependence of the lattice parameters is shown in Figure 1. The increase in the Mn content leads to a

dx.doi.org/10.1021/cm201774y |Chem. Mater. 2011, 23, 4505–4514

Table 1. Selected Parameters from the Rietveld Refinements for AP- and HP-$BiFe_{0.75}Mn_{0.25}O_3$

formula	AP-$BiFe_{0.75}Mn_{0.25}O_3$	HP-$BiFe_{0.75}Mn_{0.25}O_3$
space group	*R3c*	*Pnma*
a (Å)	5.5783(2)	5.60125(9)
b (Å)		15.6610(2)
c (Å)	13.8455(5)	11.2515(2)
Z	6	16
cell volume (Å^3)	373.11(3)	987.00(4)
calcd density (g/cm^3)	8.347	8.412
radiation	synchrotron X-rays, λ = 0.41916 Å	synchrotron X-rays, λ = 0.41916 Å
2θ range and step (deg)	$4 \le 2\theta \le 52$; 0.01	$2 \le 2\theta \le 52$; 0.01
R_I, R_P, R_{wP}	0.023, 0.039, 0.055	0.037, 0.029, 0.040

Table 2. Positional and Atomic Displacement Parameters for AP-$BiFe_{0.75}Mn_{0.25}O_3$

atom	site	*x*/*a*	*y*/*b*	*z*/*c*	U_{iso} (Å^2)
Bi	6*a*	0	0	0	0.0142(2)
FeMn1[a]	6*a*	0	0	0.22330(14)	0.0089(6)
O	18*b*	0.4507(15)	0.0194(13)	0.9539(4)	0.013(2)

[a] g = 0.75[Fe] + 0.25[Mn].

reduction in both *a* and *c* parameters. Refinement and structural parameters for AP-$BiFe_{0.75}Mn_{0.25}O_3$ are listed in Tables 1 and 2, respectively.

Oxygen hyperstoichiometry ($\delta \ge 0$) was reported for samples prepared at ambient pressure.[10,11] The δ value depends on the thermal (cooling) history, and quenching reduces δ to about 0.015(5).[10] In our work, we found that AP-$BiFe_{0.75}Mn_{0.25}O_{3+\delta}$ is oxygen stoichiometric ($\delta = -0.01(1)$) within experimental error. Note that we determined the oxygen content by TGA in 100% H_2. In ref 10, TGA in N_2 was used for the determination of oxygen nonstoichiometry.

Magnetization measurements (Figure 2a) for AP-$BiFe_{0.75}Mn_{0.25}O_3$ revealed a weak increase in the susceptibility (χ) below T_N = 485 K. This temperature falls between T_N = 520 K for x = 0.2 and T_N = 440 K for x = 0.3 determined by previous DSC measurements.[10] Above T_N, the inverse magnetic susceptibilities of AP-$BiFe_{0.75}Mn_{0.25}O_3$ follow the Curie–Weiss law $\chi = \mu_{eff}^2/[8(T - \Theta)]$. The fitting between 600 and 750 K (Figure 2) yields the effective magnetic moment μ_{eff} = 5.73μ_B and the Curie–Weiss constant Θ = −930 K ($|\Theta/T_N| \approx 1.9$). The resulting μ_{eff} is close to the expected value of 5.68μ_B for 0.75[Fe^{3+}] + 0.25[Mn^{3+}]. In a thin film of $BiFe_{0.5}Mn_{0.5}O_3$ having the same *R3c* symmetry, the μ_{eff} of 5.30μ_B was also close to the expected value of 5.43μ_B.[24] By contrast, the susceptibility of pure $BiFeO_3$ does not follow the Curie–Weiss behavior with the expected μ_{eff} of 5.916 μ_B (Figure 2a). Therefore, either the effective magnetic moment of $BiFeO_3$ deviates from the spin-only value, or this compound does not show the Curie–Weiss regime immediately above T_N.

Below T_N, the susceptibility of AP-$BiFe_{0.75}Mn_{0.25}O_3$ remains almost field-independent, as confirmed by the linear magnetization isotherm at 300 K. However, notable field dependence sets in at 220 K (Figure 3), and the **M** vs **H** loop opens at low temperatures (Figure 4b). In low magnetic fields (e.g., 100 Oe), negative magnetization is observed. Temperature-induced magnetization reversal (or negative magnetization) has been recently reported for HP-$BiFe_{0.5}Mn_{0.5}O_3$[12] and tentatively

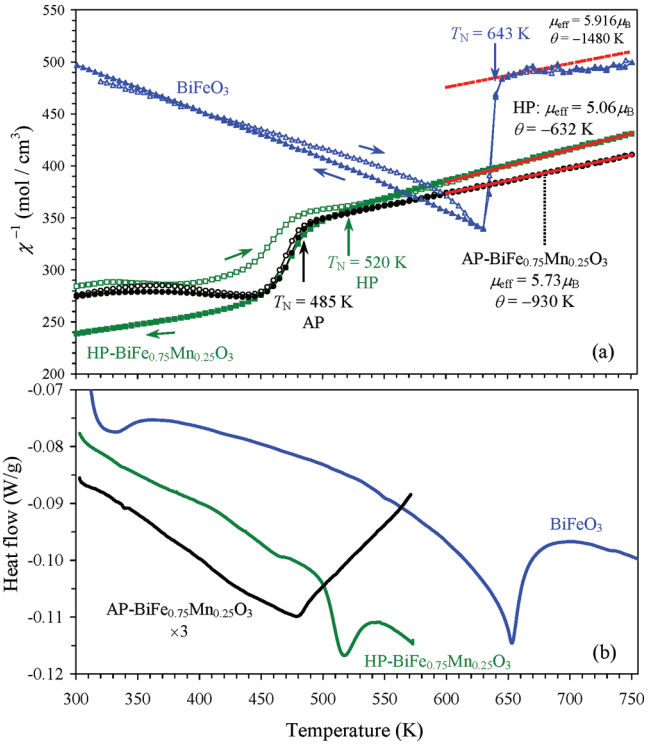

Figure 2. (a) Inverse magnetic susceptibilities of $BiFeO_3$ (at 10 kOe), AP-$BiFe_{0.75}Mn_{0.25}O_3$ (at 50 kOe), and HP-$BiFe_{0.75}Mn_{0.25}O_3$ (at 50 kOe) measured on heating from 300 to 750 K (empty symbols) and then on cooling from 750 to 300 K (filled symbols). Vertical arrows are attached to the Néel temperature, T_N. The linear curves between 600 and 750 K for AP-$BiFe_{0.75}Mn_{0.25}O_3$ and HP-$BiFe_{0.75}Mn_{0.25}O_3$ show the Curie–Weiss fits with the fitting parameters given in the figure. The dashed line for $BiFeO_3$ shows the calculated Curie–Weiss curve (not fitting results) with μ_{eff} = 5.916μ_B (the ideal value for Fe^{3+}) and Θ = −1480 K. (b) DSC curves of $BiFeO_3$ (up to 760 K), AP-$BiFe_{0.75}Mn_{0.25}O_3$ (up to 570 K), and HP-$BiFe_{0.75}Mn_{0.25}O_3$ (up to 570 K) on heating. The DSC anomalies were reproducible on cycling several times up to the mentioned temperatures.

ascribed to the competition between magnetocrystalline anisotropy and antisymmetric Dzyaloshinsky–Moriya couplings. Exchange bias behavior (a phenomenon related to magnetization reversal) was observed in nanoparticles of AP-$BiFe_{0.8}Mn_{0.2}O_3$ and attributed to surface effects.[25] Magnetization reversal behavior was reproducibly observed on ceramic samples of AP-$BiFe_{0.75}Mn_{0.25}O_3$. However, no magnetization reversal was

dx.doi.org/10.1021/cm201774y |*Chem. Mater.* 2011, 23, 4505–4514

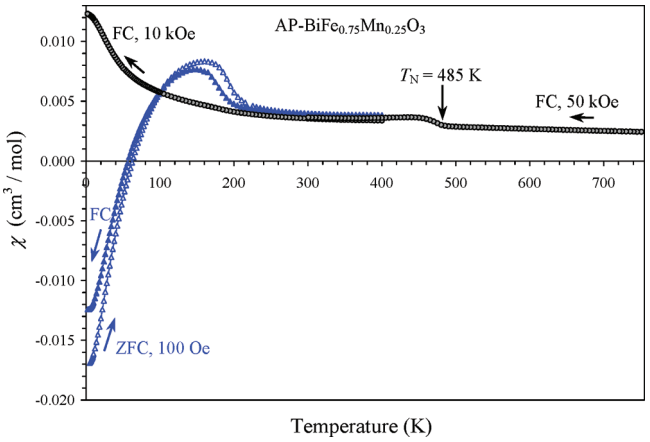

Figure 3. ZFC (empty symbols) and FC (measured on cooling; filled symbols) dc magnetic susceptibility (χ = **M**/**H**) curves of a ceramic pellet of AP-$BiFe_{0.75}Mn_{0.25}O_3$ at 100 Oe and 10 kOe. The data from 750 to 300 K were measured at 50 kOe.

found in AP-$BiFe_{0.75}Mn_{0.25}O_3$ when the same ceramic pellet was crashed into powder (see the Supporting Information). Therefore, this behavior needs further investigation.

The increase in the magnetic susceptibility below T_N has also been reported for AP-$BiFe_{0.7}Mn_{0.3}O_3$.[7] This feature, however, does not signify the formation of the net moment, since no hysteresis loop is observed at 300 K. A similar increase in χ is found for $BiFeO_3$ (Figure 2a and ref 26), although the compound does not develop a net moment down to the lowest temperatures (Figure 4a). Another similarity between $BiFeO_3$ and the AP-$BiFe_{1-x}Mn_xO_3$ phases is the formation of a long-period cycloid that has been observed in RT neutron-scattering experiments for x = 0.1 and 0.2.[6] The cancellation of the net moment may therefore persist even at high Mn dopings. However, at low temperatures the magnetic structure is likely modified and allows for new magnetic phenomena, such as the magnetization reversal and the opening of the hysteresis loop.

3.2. High-Pressure Phases. The HP-$BiFe_{0.95}Mn_{0.05}O_3$ sample crystallizes in space group *R*3*c* similarly to the AP phase. The HP-$BiFe_{0.9}Mn_{0.1}O_3$ sample was a mixture of the *R*3*c* phase and the *Pnma* phase with the $PbZrO_3$-type structure. This new structure is further developed at $0.15 \leq x \leq 0.4$. In this range of compositions, samples are dominated by the orthorhombic phase featuring the *Pnma* space group and the $\sqrt{2}a_p \times 4a_p \times 2\sqrt{2}a_p$ (a_p is the lattice parameter of a perovskite cell) superstructure (see section 3.3). The compositional dependence of the lattice parameters is shown in Figure 1. The *a* and *c* parameters decrease, while the *b* parameter increases upon doping. The HP phases have a smaller cell volume compared to their AP counterparts (e.g., for x = 0.25, V/Z(AP) = 62.02 Å^3 and V/Z(HP) = 61.66 Å^3). The cation composition of the HP-$BiFe_{0.75}Mn_{0.25}O_3$ $PbZrO_3$-type phase was confirmed by EDX analysis, which yielded the $Bi_{1.00(3)}Fe_{0.73(3)}Mn_{0.27(2)}$ formula in agreement with the nominal composition within the experimental resolution.

The HT synchrotron XRD data of HP-$BiFe_{0.75}Mn_{0.25}O_3$ are shown in Figure 5. The $\sqrt{2}a_p \times 4a_p \times 2\sqrt{2}a_p$ superstructure persists up to 500 K. Reflections from the *R*3*c* phase become clearly visible from 600 K. At 700 K, traces of the orthorhombic phase are still observed, but the majority phase has the *R*3*c* symmetry. This transition is irreversible, indicating that HP-$BiFe_{0.75}Mn_{0.25}O_3$ transforms to AP-$BiFe_{0.75}Mn_{0.25}O_3$. This

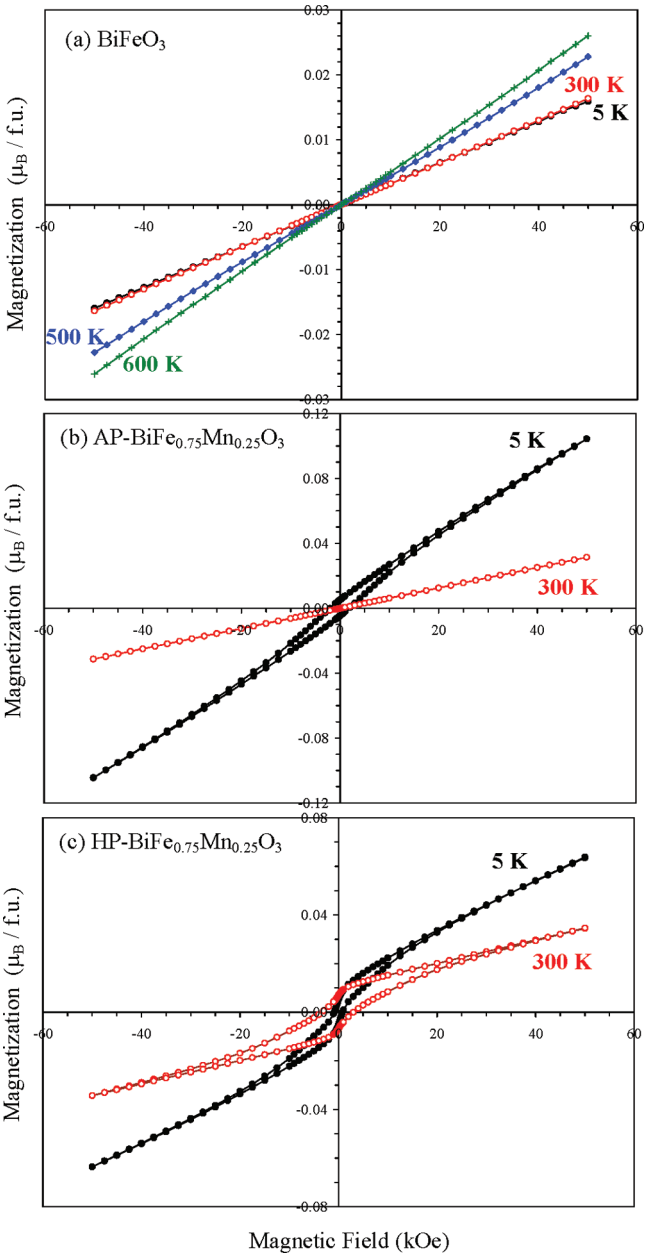

Figure 4. Isothermal magnetization curves of (a) $BiFeO_3$ (pellet), (b) AP-$BiFe_{0.75}Mn_{0.25}O_3$ (pellet), and (c) HP-$BiFe_{0.75}Mn_{0.25}O_3$ (powder) at different temperatures.

transformation was observed from about 400 K in HP-$BiFe_{0.8}Mn_{0.2}O_3$.[8] It is possible that the stability temperature of HP-$BiFe_{1-x}Mn_xO_3$ increases with increasing x.

TGA showed that HP-$BiFe_{0.75}Mn_{0.25}O_{3+\delta}$ has δ = 0.02(1). This value was calculated on the assumption that the sample is single-phase. However, the presence of a small amount of $Bi_2O_2CO_3$ impurity (see section 3.3) could affect the calculations as discussed in ref 27. To check that the oxygen content is not the primary reason for the different crystal structures of the AP and HP phases, we treated AP-$BiFe_{0.75}Mn_{0.25}O_3$ at the same HP synthesis conditions and observed the transformation into HP-$BiFe_{0.75}Mn_{0.25}O_3$.

Despite several impurity phases identified by our structure refinement (section 3.3), the basic features of the magnetic

dx.doi.org/10.1021/cm201774y |*Chem. Mater.* 2011, 23, 4505–4514

behavior could be determined. The $Bi_2O_2CO_3$ impurity is diamagnetic, whereas trace amounts of $Bi_{25}(Fe,Mn)O_{39+\delta}$ produce a negligible paramagnetic contribution due to the strong dilution of magnetic ions. Finally, the contribution of AP-$BiFe_{0.75}Mn_{0.25}O_3$ can be accounted for by the data presented in section 3.1. In contrast to the AP phase, HP-$BiFe_{0.75}Mn_{0.25}O_3$ shows a divergence of the ZFC and FC curves below 530 K. The DSC anomaly at nearly the same temperature confirmed the phase transition and the magnetic ordering (Figure 2b). This DSC anomaly is reproducible without any changes on cycling (four cycles were performed) between 290 and 570 K, and it disappears after heating to 870 K. The Curie−Weiss fit between 600 and 750 K leads to $\mu_{eff} = 5.06\mu_B$ and $\Theta = -632$ K, with a somewhat underestimated effective moment (compare to $5.68\mu_B$ expected for $0.75[Fe^{3+}] + 0.25[Mn^{3+}]$). According to the HT synchrotron XRD data, the AP phase clearly appears above about 600 K. Therefore, HP-$BiFe_{0.75}Mn_{0.25}O_3$ should include a magnetic contribution from the AP phase above 600 K and on cooling from 750 K. (XRD data collected after the magnetization measurement up to 750 K indeed showed that the main phase had *R*3*c* symmetry.) Magnetic anomalies near 460−480 K in HP-$BiFe_{0.75}Mn_{0.25}O_3$ originate from the presence of AP-$BiFe_{0.75}Mn_{0.25}O_3$. Below T_N, the divergence of the FC and ZFC curves (Figure 2a), the field dependence of the susceptibility, and the hysteresis loops in magnetization isotherms (Figure 4c) identify HP-$BiFe_{0.75}Mn_{0.25}O_3$ as a canted antiferromagnet with a net moment of about $0.01\mu_B$/f.u. at 5 K.

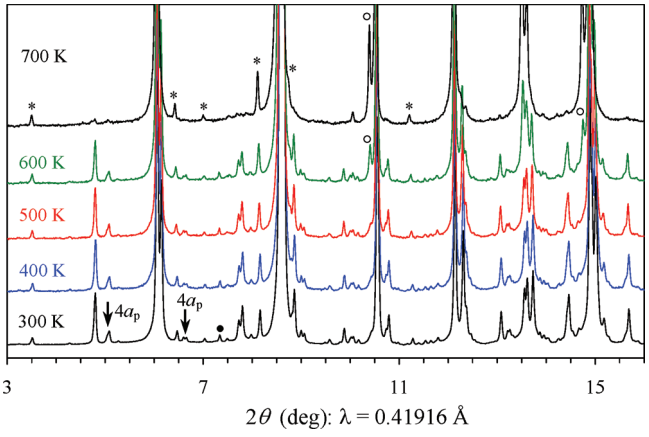

Figure 5. High-temperature synchrotron X-ray powder diffraction patterns of HP-$BiFe_{0.75}Mn_{0.25}O_3$. Asterisks show reflections from the $Bi_2O_2CO_3$ impurity. A black circle shows the strongest reflection from the $Bi_{25}(Fe,Mn)O_{39+\delta}$ impurity. Arrows are attached to some reflections corresponding to the $b = 4a_p$ superstructure. The white circles at 600 and 700 K show the characteristic reflections (which do not overlap with reflections from the *Pnma* phase) of the *R*3*c* phase.

3.3. Crystal Structure of HP-$BiFe_{0.75}Mn_{0.25}O_3$. Electron diffraction patterns of HP-$BiFe_{0.75}Mn_{0.25}O_3$ (Figure 6) clearly show the orthorhombic unit cell with the lattice parameters $a = a_p\sqrt{2}$, $b = 4a_p$, and $c = 2a_p\sqrt{2}$ and space group *Pnma* or its acentric subgroup $Pn2_1a$. When the parent cubic perovskite structure is transformed to the supercell, every position of the inversion center in the perovskite structure can be chosen as a potential origin of the supercell. All these possibilities were tested for compatibility with the *Pnma* space symmetry. The only variants, matching with the simultaneous presence of the *n* and *a* glide planes, are those where the origin of the supercell is chosen either at the center of the face of the perovskite unit cell (position 1/2, 1/2, 0 or 0, 1/2, 1/2) or at the oxygen atoms in the *ac* plane (position 1/2, 0, 0 or 0, 0, 1/2). These possibilities result in a different arrangement of the atomic species with respect to the symmetry elements of the *Pnma* space group and, hence, in different structures. When the symmetry is reduced to $Pn2_1a$, these structures become symmetrically identical because the position of the origin along the *b*-axis can be arbitrarily chosen in this space group.

The aforementioned structural models have been tested in the Rietveld refinement. The model with the origin at 1/2, 0, 0 led to an unacceptably high reliability factor $R_I = 0.082$ and abnormally large atomic displacement parameters (ADPs) for some oxygen atoms. Therefore, this model was rejected. The final refinement of the model with the origin choice at 1/2, 1/2, 0 was performed with common ADPs for the Bi, (Fe,Mn), and O atoms, respectively. The occupancies of the B-positions were fixed at $0.75[Fe] + 0.25[Mn]$. Impurity phases were introduced into the refinement: $Bi_2O_2CO_3$ ($a = 3.8670(3)$ Å, $c = 13.689(2)$ Å, space group *I*4/*mmm*, 2.56(4) wt %, $R_I = 0.040$) and $Bi_{25}(Fe,Mn)O_{39+\delta}$ ($a = 10.381(2)$ Å, space group *I*23, 0.47(3) wt %, $R_I = 0.041$). A close inspection of the difference curve after the Rietveld refinement revealed broad shoulders on the low-angle side of the perovskite subcell reflections (see also Figure 5 near $2\theta \approx 10.4°$). These shoulders were taken into account by introducing the *R*3*c* AP-$BiFe_{0.75}Mn_{0.25}O_3$ phase into the refinement ($a = 5.596(1)$Å, $c = 13.878(5)$Å, 15.1(3) wt %, $R_I = 0.020$) (Figure S1 of the Supporting Information). This significantly improved the quality of the fit and reduced R_P from 0.041 to 0.029. Approximately the same amount of the *R*3*c* phase could be detected in HP-$BiFe_{1-x}Mn_xO_3$ for $0.15 \le x \le 0.25$ when the *R*3*c* phase was introduced into Rietveld refinements. HP-$BiFe_{0.9}Mn_{0.1}O_3$ contained a significantly larger amount of the *R*3*c* phase (about 40%), and reflections from the *R*3*c* phase could be clearly observed (see the Supporting Information). The reason why

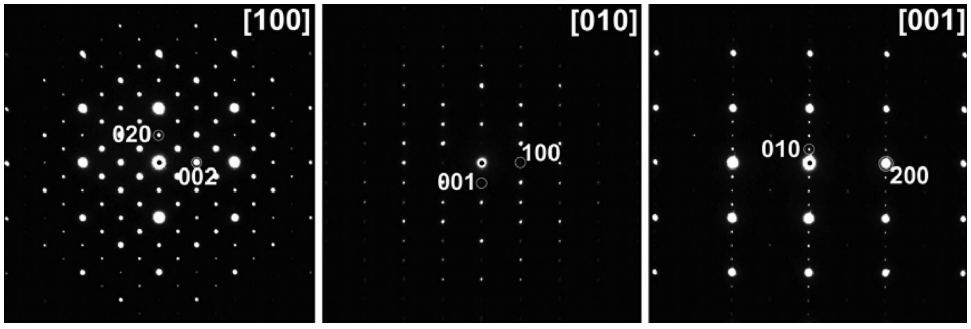

Figure 6. Electron diffraction patterns of HP-$BiFe_{0.75}Mn_{0.25}O_3$.

dx.doi.org/10.1021/cm201774y |*Chem. Mater.* 2011, 23, 4505–4514

Table 3. Positional and Atomic Displacement Parameters for HP-$BiFe_{0.75}Mn_{0.25}O_3$

atom	site	x/a	y/b	z/c	U_{iso} (Å^2)
Bi1	8*d*	0.2025(4)	0.01057(9)	0.6269(2)	0.0148(2)
Bi2	4*c*	0.2054(7)	1/4	0.6255(7)	=*U*(Bi1)
Bi3	4*c*	0.7801(6)	1/4	0.3611(2)	=*U*(Bi1)
FeMn1[a]	8*d*	0.246(1)	0.1223(5)	0.8799(7)	0.0147(5)
FeMn2[a]	8*d*	0.250(1)	0.6239(5)	0.8779(7)	=*U*(FeMn1)
O1	8*d*	0.805(4)	0.004(1)	0.669(2)	0.004(2)
O2	4*c*	0.789(7)	1/4	0.626(3)	=*U*(O1)
O3	4*c*	0.191(7)	1/4	0.419(3)	=*U*(O1)
O4	8*d*	0.081(4)	0.131(2)	0.725(2)	=*U*(O1)
O5	8*d*	−0.039(4)	0.389(2)	−0.020(2)	=*U*(O1)
O6	8*d*	0.048(4)	0.652(2)	0.747(2)	=*U*(O1)
O7	8*d*	−0.009(1)	0.406(3)	0.483(3)	=*U*(O1)

[a] $g = 0.75[Fe] + 0.25[Mn]$.

Table 4. Selected Interatomic Distances and Bond Valence Sums (BVSs) for HP-$BiFe_{0.75}Mn_{0.25}O_3$

Bi1−O1	2.28(2) × 1	Bi3−O2	2.98(4) × 1
Bi1−O1	2.37(2) × 1	Bi3−O3	2.39(4) × 1
Bi1−O1	3.34(2) × 1	Bi3−O3	3.19(4) × 1
Bi1−O1	3.41(2) × 1	Bi3−O3	3.36(4) × 1
Bi1−O4	2.29(3) × 1	Bi3−O5	3.34(2) × 2
Bi1−O4	3.30(2) × 1	Bi3−O6	2.18(2) × 2
Bi1−O5	2.45(2) × 1	Bi3−O6	2.71(2) × 2
Bi1−O5	3.14(2) × 1	Bi3−O7	3.04(2) × 2
Bi1−O6	3.01(2) × 1	BVS = 2.79(9)	
Bi1−O6	3.50(2) × 1		
Bi1−O7	2.31(2) × 1	FeMn1−O1	1.96(2) × 1
Bi1−O7	2.39(3) × 1	FeMn1−O2	2.016(9) × 1
BVS = 3.31(8)		FeMn1−O4	1.98(2) × 1
		FeMn1−O4	2.22(2) × 1
Bi2−O2	2.33(4) × 1	FeMn1−O5	1.96(2) × 1
Bi2−O2	2.83(4) × 1	FeMn1−O7	2.12(3) × 1
Bi2−O2	3.27(4) × 1	BVS = 2.89(7)	
Bi2−O3	2.32(4) × 1		
Bi2−O4	2.28(3) × 2	FeMn2−O1	2.10(2) × 1
Bi2−O4	3.27(2) × 2	FeMn2−O3	2.06(1) × 1
Bi2−O5	2.87(2) × 2	FeMn2−O5	2.01(1) × 1
Bi2−O7	3.17(2) × 2	FeMn2−O6	1.91(3) × 1
BVS = 2.9(1)		FeMn2−O6	2.23(3) × 1
		FeMn2−O7	1.93(3) × 1
		BVS = 2.95(8)	

the *R*3*c* phase remains in the samples with $0.15 \leq x \leq 0.25$ needs further study. The crystallographic parameters and positional and atomic displacement parameters of HP-$BiFe_{0.75}Mn_{0.25}O_3$ are listed in Tables 1 and 3, respectively. Main interatomic distances are presented in Table 4. Experimental, calculated, and difference diffraction profiles are shown in Figure 7. The refinement in the $Pn2_1a$ space group did not improve the reliability factors and resulted in atomic coordinates very close to those in the *Pnma* model.

The crystal structure of HP-$BiFe_{0.75}Mn_{0.25}O_3$ is shown in Figure 8. The Fe and Mn atoms are situated in distorted oxygen

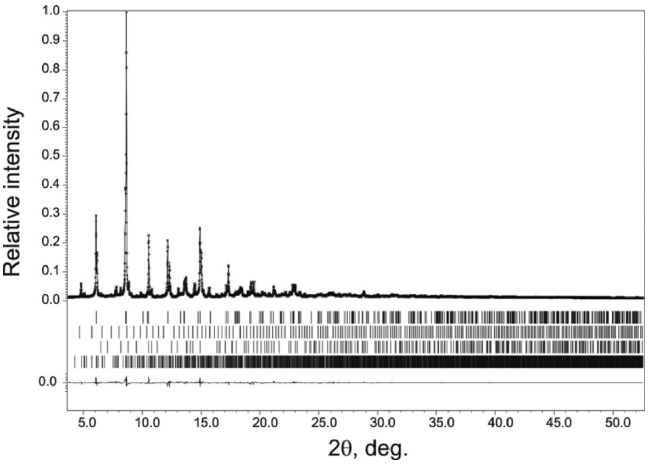

Figure 7. Experimental, calculated, and difference synchrotron XRD profiles for HP-$BiFe_{0.75}Mn_{0.25}O_3$. The bars mark the reflection positions (from top to bottom) for the *R*3*c* phase, $Bi_{25}(Fe,Mn)O_{39+\delta}$, $Bi_2O_2CO_3$, and HP-$BiFe_{0.75}Mn_{0.25}O_3$.

octahedra. The perovskite octahedral framework is subjected to strong distortion due to a cooperative tilting of the octahedral units. The tilting pattern can be described as consisting of two components. The primary tilt system is $a^-b^0a^-$. An additional tilt occurs around the *b*-axis, but instead of conventional b^+ (in-phase tilt) or b^- (out-of-phase tilt) components, the octahedra with the same tilt direction are grouped into pairs, resulting in the *oioi* sequence along the *b*-axis (*o* and *i* stand for the out-of-phase and in-phase tilts, respectively). This results in the $b = 4a_p$ superstructure.

The geometry of the octahedral oxygen environment around the FeMn1 and FeMn2 atoms is virtually identical. The transition-metal cations are shifted from the centers of the octahedra, making one metal−oxygen bond substantially longer (2.22−2.23 Å) than the remaining five bonds (1.91−2.12 Å) (Figure 9). This elongation might be necessary to compensate for short bonds linking the respective O4 and O6 atoms to the neighboring Bi2 and Bi3 atoms (2.18−2.28 Å). The formation of strong covalent Bi−O bonds is typically related to a localization of the lone electron pair on Bi^{3+} cations and the ensuing displacement of Bi atoms. Indeed, ELF reveals well-defined maxima in the vicinity of the Bi sites. Such maxima are usually ascribed to localized lone pairs.[23] Figure 10 shows the arrangement of ELF isosurfaces along with the O4 and O6 atoms located opposite the lone pair and, therefore, forming short bonds to the Bi atoms. Antiparallel displacements of the Bi atoms along the $\pm[100]$ (equal to $\pm\langle 110\rangle_p$) direction are in agreement with this picture. On going along the *c* axis, the displacements of the Bi atoms follow the sequence ↑↑↓↓, where ↑ denotes a shift in the [100] direction and ↓ denotes a shift in the $[\bar{1}00]$ direction. This displacement pattern leads to the doubling of the $c = 2a_p\sqrt{2}$ lattice parameter compared to the $a_p\sqrt{2}$ imposed by the $a^-b^0a^-$ tilting system.

The crystal structure of HP-$BiFe_{0.75}Mn_{0.25}O_3$ was confirmed by HAADF-STEM and ABF-STEM observations. The [100] HAADF-STEM image corresponds to the $\{110\}_p$ projection of the perovskite subcell (Figure 11). The prominent pattern of bright dots on the image reproduces the projection of the Bi atomic columns as they are shown on the [100] structure projection in Figure 8. The dots on the image form two types of layers. The layer of the first type is completely flat, with the Bi2

dx.doi.org/10.1021/cm201774y |*Chem. Mater.* 2011, 23, 4505–4514

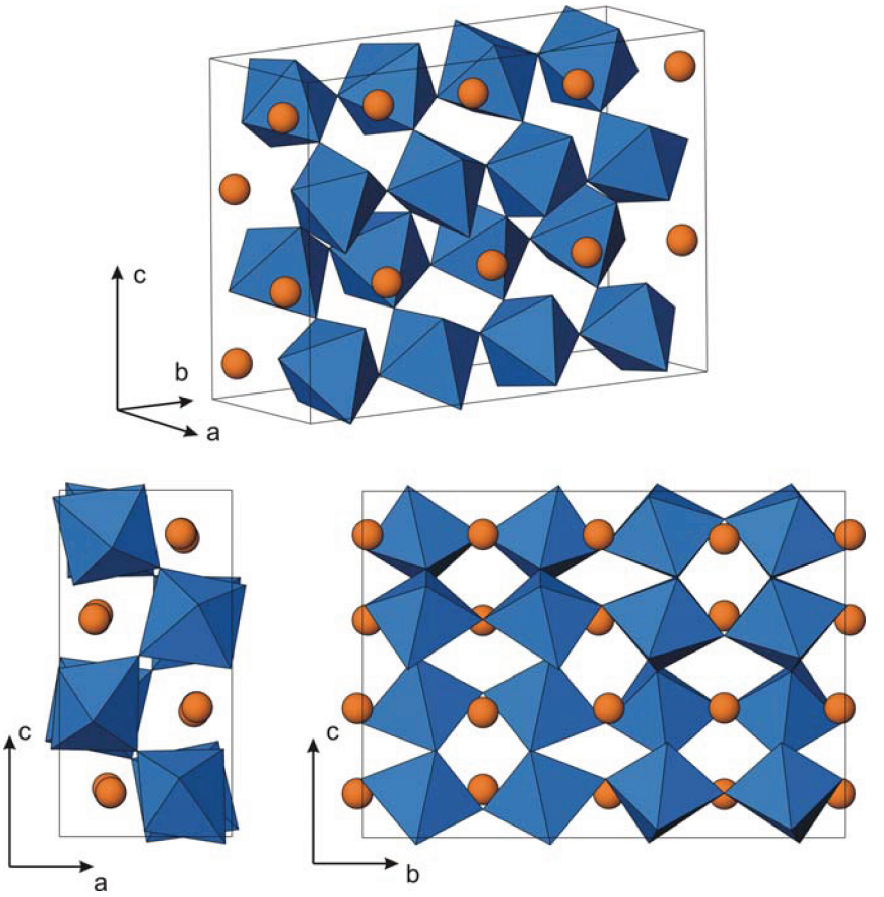

Figure 8. Different projections of the crystal structure of HP-$BiFe_{0.75}Mn_{0.25}O_3$. The Fe/Mn atoms are situated in octahedra, and the Bi atoms are shown as spheres.

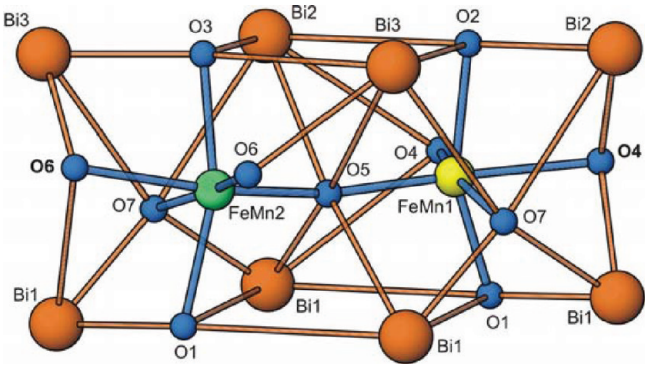

Figure 9. Scheme of the metal−oxygen bonds in HP-$BiFe_{0.75}Mn_{0.25}O_3$. The oxygen atoms forming elongated bonds to the FeMn1 and FeMn2 atoms are marked in bold.

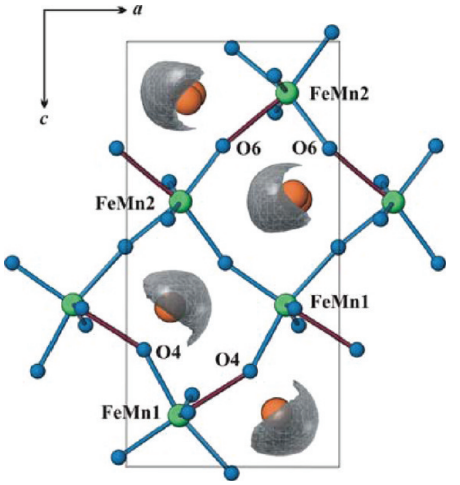

Figure 10. Projection of the HP-$BiFe_{0.75}Mn_{0.25}O_3$ structure with long FeMn−O bonds colored in brown. Shaded lobes depict ELF (η) isosurfaces for $\eta = 0.7$.

and Bi3 atoms positioned at the $y = 1/4$ and 3/4 mirror planes, which inhibits their displacement along the *c*-axis. The layers of the second type comprise Bi1 atoms only and are located at $y \approx 0$, 1/2. The layer appears clearly corrugated on the HAADF-STEM image, with alternating pairs of Bi atoms shifted above and below the $y = 0$, 1/2 planes. These shifts are well visible on the structure projection (Figure 8). The displacement of the Bi1 atoms from the $y = 0$, 1/2 planes was quantitatively estimated from the HAADF-STEM image. This was done by measuring intensity profiles of the atomic rows along the *y*-direction. The profiles were fitted with a set of Gaussian peaks in the Fityk software.[28] The measured displacement $\Delta y = 0.17(5)$ Å is in good agreement with $\Delta y = 0.166$ Å calculated from the atomic coordinate *y*(Bi1) (Table 3). The calculated HAADF-STEM image (thickness $t = 7.2$ nm) is in excellent agreement with the experimental one.

dx.doi.org/10.1021/cm201774y |*Chem. Mater.* 2011, 23, 4505–4514

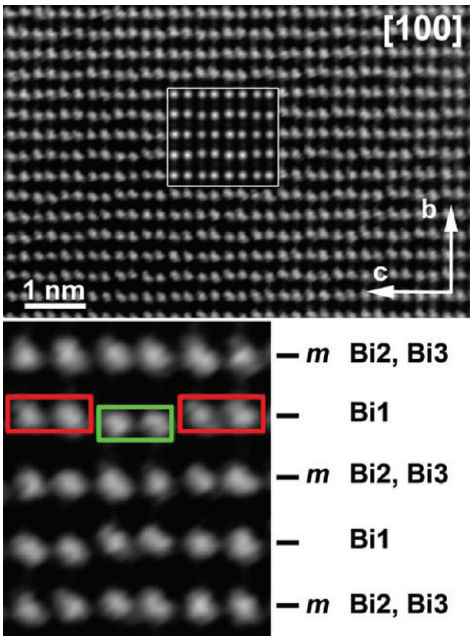

Figure 11. [100] HAADF-STEM image of the HP-$BiFe_{0.75}Mn_{0.25}O_3$ structure (top). The calculated HAADF-STEM image (t = 7.2 nm) is shown as an inset and outlined with a white border. At the bottom is the enlarged part of the image with indication of the two types of Bi layers. The alternating pairs of Bi atoms shifted above and below the y = 0 and 1/2 planes are marked with red and green rectangles, respectively.

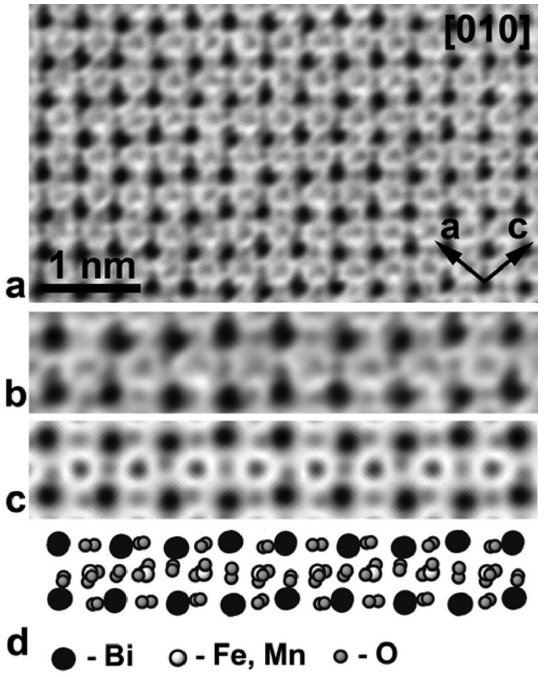

Figure 12. [010] ABF-STEM image of the HP-$BiFe_{0.75}Mn_{0.25}O_3$ structure (a). The enlarged strip of the image, calculated ABF-STEM image (t = 8 nm), and corresponding structure projection are provided in panels b, c, and d, respectively.

The oxygen sublattice is visualized using the ABF-STEM technique. The ABF-STEM images demonstrate an "absorptive" type of contrast, where the regions of higher atomic potential look darker on a bright background. Due to the impact of elastic scattering, columns of light elements can be observed more easily together with the heavy atomic columns on ABF-STEM images, in contrast to HAADF-STEM images.[29,30] A high-pass-filtered [010] ABF-STEM image of the HP-$BiFe_{0.75}Mn_{0.25}O_3$ structure is shown in Figure 12a (the original image is provided in Figure S2 of the Supporting Information). An enlarged strip of the image is presented in Figure 12b along with the calculated ABF-STEM image (t = 8 nm, Figure 12c) and the corresponding structure projection (Figure 12d). The experimental image perfectly reproduces the projected positions of the oxygen columns as well as the wavy position modulation of the Bi layers.

4. DISCUSSION

HP-$BiFe_{0.75}Mn_{0.25}O_3$ has the same superstructure as $Bi_{0.82}La_{0.18}FeO_3$[31] and $Bi_{0.85}Nd_{0.15}FeO_3$[32−35] (according to electron diffraction observations). It is interesting that the substitutions in either the Bi sublattice or the Fe sublattice result in the same superstructure. In HP-$BiFe_{0.5}Mn_{0.5}O_3$,[12] a similar $PbZrO_3$-type $\sqrt{2}a_p \times 2\sqrt{2}a_p \times 2a_p$ superstructure was detected by electron diffraction, however, with an uncertainty in the c-parameter value due to multitwinning effects. We may conjecture that the range of HP-$BiFe_{1-x}Mn_xO_3$ phases continuously extends to x = 0.5 and HP-$BiFe_{0.5}Mn_{0.5}O_3$ has the same $\sqrt{2}a_p \times 2\sqrt{2}a_p \times 4a_p$ supercell. Additionally, we argue that the structure of HP-$BiFe_{0.75}Mn_{0.25}O_3$ has no prerequisites for the Fe^{3+}/Mn^{3+} ordering, in contrast to the recent claim of ref 12 on the possible cation ordering at x = 0.5. Indeed, the subtle difference in the coordination environment of the FeMn1 and FeMn2 cations in HP-$BiFe_{0.75}Mn_{0.25}O_3$ is unlikely to provide sufficient energy gain for inducing the ordering of B-cations. Moreover, the observation of the same $\sqrt{2}a_p \times 2\sqrt{2}a_p \times 4a_p$ superstructure in the Mn-free perovskites $Bi_{0.82}La_{0.18}FeO_3$[31] and $Bi_{0.85}Nd_{0.15}FeO_3$[32−35] makes it clear that the inherent Jahn−Teller distortion of Mn^{3+} cannot be the main driving force for the formation of this superstructure.

The HP-$BiFe_{0.75}Mn_{0.25}O_3$ structure can be compared with the room-temperature antiferroelectrics $PbZrO_3$ and $NaNbO_3$.[36,37] The antiferrodistorsive instability in $PbZrO_3$ originates primarily from the Pb and O displacements, with a smaller contribution of the Zr displacements (see Figure 13, where the $PbZrO_3$ structure is shown in the *Pcma* setting of the *Pbam* space group for an easier comparison with the HP-$BiFe_{0.75}Mn_{0.25}O_3$ and $NaNbO_3$ structures).[38] The Pb and O atoms are shifted along the $\pm$[100] (equal to $\pm\langle 110\rangle_p$) direction of the orthorhombic unit cell and alternate along [001] following the ↑↑↓↓ pattern (a displacement associated with the Σ_3 mode in Cowley's tables).[39] According to the tolerance factor t = 0.963, the $PbZrO_3$ structure is additionally subjected to an octahedral tilting distortion of the $a^-b^0a^-$ type (the R-point instability, R_{25} mode). In the room-temperature structure of $NaNbO_3$ (t = 0.967), the same $a^-b^0a^-$ tilting distortion is accompanied by an alternating *oioi* sequence of the in-phase and out-of-phase octahedral tilts about the b-axis (see Figure 13; the structure is represented in the *Pbma* setting according to ref 37). More generally, the room-temperature $NaNbO_3$ structure can be considered as the δ = 1/4 point in the series of commensurately modulated phases with the [1/2, δ, 1/2] (δ = 1/4, 1/6, 1/12) modulation vectors. These modulation vectors correspond to the in-phase and out-of-phase tilt sequences $(oi)_2$, $(ooi)_2$, and $(ooooii)_2$ arising from a combination of the M_3 (in-phase rotations) and R_{25} (out-of-phase rotations) modes with a weak coupling between the rotations

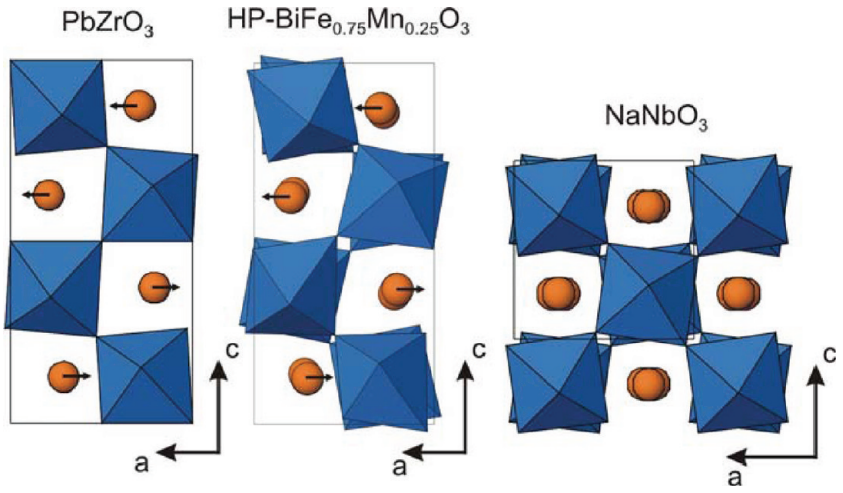

Figure 13. Comparison of the $PbZrO_3$, HP-$BiFe_{0.75}Mn_{0.25}O_3$, and $NaNbO_3$ structures. A-cations are shown as spheres. Small arrows mark the directions of antiparallel displacements of the Pb and Bi atoms.

in the neighboring layers along the *b*-axis.[40,41] Off-center displacements of the Nb atoms along $\langle 110 \rangle_p$ form an antiferroelectric pattern without significant contribution of the Na displacements.

The HP-$BiFe_{0.75}Mn_{0.25}O_3$ structure comprises features of both the $PbZrO_3$ and $NaNbO_3$ superstructures: (i) the Σ_3-type antiferroelectric shift of the Bi atoms along $\pm[100]$, (ii) the $a^-b^0a^-$ tilting distortion, and (iii) the alternating *oioi* sequence of the in-phase and out-of-phase octahedral tilts around the *b*-axis. The deformation of the $(Fe,Mn)O_6$ octahedra in HP-$BiFe_{0.75}Mn_{0.25}O_3$ further resembles the $PbZrO_3$ structure, where one of the oxygen atoms forming the longest Zr−O bond of about 2.17 Å is simultaneously involved in the shortest Pb−O contact. This supports our conjecture that the deformation of the octahedron is primarily driven by the covalent Bi(Pb)−O bonding and related stereochemical activity of the lone pair, as confirmed by the ELF analysis for HP-$BiFe_{0.75}Mn_{0.25}O_3$. The octahedral deformation in HP-$BiFe_{0.75}Mn_{0.25}O_3$ can be boosted by the Jahn−Teller effect for the Mn^{3+} cations, but the formation of similar superstructures in $PbZrO_3$, $Bi_{0.82}La_{0.18}FeO_3$, $Bi_{0.85}Nd_{0.15}FeO_3$, $BiMnO_{3.16}$,[27] $Bi_2Mn_{4/3}Ni_{2/3}O_6$,[42] and $BiScO_3$ (in thin films)[43] indicates that the nature of the B-cation is of secondary importance.

Another issue concerns the possible origins of the complex $(oi)_2$ in-phase and out-of-phase octahedral tilt sequence and its coupling to antiferroelectric A-cation displacements. The presence of such tilting pattern in $NaNbO_3$ and the damping of the tilts around the *b*-axis in $PbZrO_3$ show that the antiferroelectric displacements of the lone-pair A-cations actually suppress the tilting distortion, especially taking into account very close tolerance factors (t = 0.967, 0.963) for the two compounds. The emergence of this tilting component in the HP-$BiFe_{0.75}Mn_{0.25}O_3$, $Bi_{0.82}La_{0.18}FeO_3$, and $Bi_{0.85}Nd_{0.15}FeO_3$ structures might be related to a reduced tolerance factor (t = 0.922, 0.920, and 0.915, respectively). However, a detailed atomistic model of the interplay among the octahedral tilts, octahedral distortions, and lone-pair cation displacements requires accurate ab initio calculations and should be a subject of future work.

The transformation of the AP-$BiFe_{0.75}Mn_{0.25}O_3$ room-temperature ferroelectric *R*3*c* phase into the HP-$BiFe_{0.75}Mn_{0.25}O_3$ antiferroelectric *Pnma* phase at 6 GPa implies a pressure-induced phase transition (or a sequence of phase transitions) between these two polymorphs. Apparently, the tendency of the $(Fe,Mn)O_6$ octahedra to deform due to an increasing concentration of Mn^{3+} Jahn−Teller cations plays a role in shifting the stability range of the antiferroelectric phase toward lower pressure. Indeed, we observed that $BiFe_{0.95}Mn_{0.05}O_3$ retains the *R*3*c* structure even after the high-temperature treatment at 6 GPa. One can expect a complex sequence of phase transitions under pressure in the $BiFe_{1-x}Mn_xO_3$ system due to the interplay among lone-pair-driven (anti)ferroelectric displacements, octahedral deformation, and the octahedral tilting pattern similar to the complicated HP behavior of $BiFeO_3$.[44,45] In situ high-pressure high-resolution diffraction experiments are necessary to unravel the behavior of the $BiFe_{1-x}Mn_xO_3$ solid solutions under pressure.

In summary, we have presented the structure and magnetic properties of ambient-pressure and high-pressure $BiFe_{1-x}Mn_xO_3$ solid solutions. The structure of the orthorhombic $PbZrO_3$-type phase observed in several $BiFeO_3$-based solid solutions was studied in detail. This structure is antiferroelectric and combines an intricate octahedral tilting pattern with displacements of the Bi atoms and deformations of the $(FeMn)O_6$ octahedra. The transformation of the ferroelectric *R*3*c* structure into this new type of superstructure induces a weak net magnetic moment, but simultaneously converts the ferroelectric structure into an antiferroelectric one, thereby canceling the net electric polarization. While this transformation is unfavorable for multiferroicity, new interesting properties, such as the magnetization reversal in HP-$BiFe_{0.5}Mn_{0.5}O_3$,[12] emerge. Surprisingly, a similar effect is observed in AP-$BiFe_{0.75}Mn_{0.25}O_3$ and presents an interesting field for future studies.

■ ASSOCIATED CONTENT

Supporting Information. Full ref 42, comparison of the Rietveld refinement of the HP-$BiFe_{0.75}Mn_{0.25}O_3$ phase with and without introduction of the *R*3*c* phase, unfiltered [010] ABF-STEM image of HP-$BiFe_{0.75}Mn_{0.25}O_3$, XRD patterns, details of the HT synchrotron XRD patterns, specific heat data, magnetization data, and dielectric data (PDF) and CIF file for HP-$BiFe_{0.75}Mn_{0.25}O_3$. This material is available free of charge via the Internet at http://pubs.acs.org.

AUTHOR INFORMATION

Corresponding Author
*E-mail: Alexei.Belik@nims.go.jp.

ACKNOWLEDGMENT

This work was supported by the World Premier International Research Center Initiative (WPI Initiative, MEXT, Japan), the NIMS Individual-Type Competitive Research Grant, the Japan Society for the Promotion of Science (JSPS) through its Funding Program for World-Leading Innovative R&D on Science and Technology (FIRST Program), and a Grant-in-Aid for Scientific Research (22246083) from JSPS, Japan. The synchrotron radiation experiments were performed at the SPring-8 with the approval of the Japan Synchrotron Radiation Research Institute (Proposal Numbers 2009A1136 and 2010A1215). We thank Dr. T. Kolodiazhnyi of NIMS for his help with the TGA experiment in hydrogen. A.A.T. was funded by the Alexander von Humboldt Foundation. A.M.A., J.H., and G.V.T. appreciate the financial help of the Hercules Foundation. J.H. acknowledges financial support from the Research Foundation−Flanders (FWO G.0184.09N).

REFERENCES

(1) Catalan, G.; Scott, J. F. *Adv. Mater.* **2009**, *21*, 2463.
(2) Wang, J.; Neaton, J. B.; Zheng, H.; Nagarajan, V.; Ogale, S. B.; Liu, B.; Viehland, D.; Vaithyanathan, V.; Schlom, D. G.; Waghmare, U. V.; Spaldin, N. A.; Rabe, K. M.; Wuttig, M.; Ramesh, R. *Science* **2003**, *299*, 1719.
(3) Hill, N. A. *J. Phys. Chem. B* **2000**, *104*, 6694.
(4) (a) Kawae, T.; Terauchi, Y.; Tsuda, H.; Kumeda, M.; Morimoto, A. *Appl. Phys. Lett.* **2009**, *94*, 112904. (b) Wang, S. Y.; Qiu, X.; Gao, J.; Feng, Y.; Su, W. N.; Zheng, J. X.; Yu, D. S.; Li, D. J. *Appl. Phys. Lett.* **2011**, *98*, 152902.
(5) Khomchenko, V. A.; Kiselev, D. A.; Bdikin, I. K.; Shvartsman, V. V.; Borisov, P.; Kleemann, W.; Vieira, J. M.; Kholkin, A. L. *Appl. Phys. Lett.* **2008**, *93*, 262905.
(6) Sosnowska, I.; Schäfer, W.; Kockelmann, W.; Andersen, K. H.; Troyanchuk, I. O. *Appl. Phys. A: Mater. Sci. Process.* **2002**, *74*, S1040.
(7) Yang, C.-H.; Koo, T. Y.; Jeong, Y. H. *Solid State Commun.* **2005**, *134*, 299.
(8) Azuma, M.; Kanda, H.; Belik, A. A.; Shimakawa, Y.; Takano, M. *J. Magn. Magn. Mater.* **2007**, *310*, 1177.
(9) Sahu, J. R.; Rao, C. N. R. *Solid State Sci.* **2007**, *9*, 950.
(10) Selbach, S. M.; Tybell, T.; Einarsrud, M. A.; Grande, T. *Chem. Mater.* **2009**, *21*, 5176.
(11) Selbach, S. M.; Tybell, T.; Einarsrud, M. A.; Grande, T. *Phys. Rev. B* **2009**, *79*, 214113.
(12) Mandal, P.; Sundaresan, A.; Rao, C. N. R.; Iyo, A.; Shirage, P. M.; Tanaka, Y.; Simon, C.; Pralong, V.; Lebedev, O. I.; Caignaert, V.; Raveau, B. *Phys. Rev. B* **2010**, *82*, 100416.
(13) Moreira dos Santos, A.; Cheetham, A. K.; Atou, T.; Syono, Y.; Yamaguchi, Y.; Ohoyama, K.; Chiba, H.; Rao, C. N. R. *Phys. Rev. B* **2002**, *66*, 064425.
(14) Wen, F. S.; Wang, N.; Zhang, F. *Solid State Commun.* **2010**, *150*, 39.
(15) Su, W. N.; Wang, D. H.; Cao, Q. Q.; Han, Z. D.; Yin, J.; Zhang, J. R.; Du, Y. W. *Appl. Phys. Lett.* **2007**, *91*, 092905.
(16) Suchomel, M. R.; Thomas, C. I.; Allix, M.; Rosseinsky, M. J.; Fogg, A. M.; Thomas, M. F. *Appl. Phys. Lett.* **2007**, *90*, 112909.
(17) Azuma, M.; Niitaka, S.; Hayashi, N.; Oka, K.; Takano, M.; Funakubo, H.; Shimakawa, Y. *Jpn. J. Appl. Phys.* **2008**, *47*, 7579.
(18) Nishibori, E.; Takata, M.; Kato, K.; Sakata, M.; Kubota, Y.; Aoyagi, S.; Kuroiwa, Y.; Yamakata, M.; Ikeda, N. *Nucl. Instrum. Methods Phys. Res., Sect. A* **2001**, *467−468*, 1045.
(19) Petricek, V.; Dusek, M. *The Crystallographic Computing System JANA2006*; Institute of Physics: Praha, Czech Republic, 2006.
(20) Koch, C. Determination of Core Structure Periodicity and Point Defect Density along Dislocations. Ph.D. Thesis, Arizona State University, 2002.
(21) Andersen, O. K.; Pawlowska, Z.; Jepsen, O. *Phys. Rev. B* **1986**, *34*, 5253.
(22) Perdew, J. P.; Wang, Y. *Phys. Rev. B* **1992**, *45*, 13244.
(23) For example, see: Seshadri, R.; Hill, N. A. *Chem. Mater.* **2001**, *13*, 2892.
(24) Du, Y.; Cheng, Z. X.; Dou, S. X.; Wang, X. L.; Zhao, H. Y.; Kimura, H. *Appl. Phys. Lett.* **2010**, *97*, 122502.
(25) Manna, P. K.; Yusuf, S. M.; Shukla, R.; Tyagi, A. K. *Phys. Rev. B* **2011**, *83*, 184412.
(26) (a) Ramazanoglu, M.; Ratcliff, W., II; Choi, Y. J.; Lee, S.; Cheong, S. W.; Kiryukhin, V. *Phys. Rev. B* **2011**, *83*, 174434. (b) Roginskaya, Yu. E.; Venevtsev, Yu. N.; Fedotov, S. A.; Zhdanov, G. S. *Sov. Phys. Crystallogr.* **1964**, *8*, 490.
(27) Belik, A. A.; Kolodiazhnyi, T.; Kosuda, K.; Takayama-Muromachi, E. *J. Mater. Chem.* **2009**, *19*, 1593.
(28) Wojdyr, M. *J. Appl. Crystallogr.* **2010**, *43*, 1126.
(29) Findlay, S. D.; Shibata, N.; Sawada, H.; Okunishi, E.; Kondo, Y.; Yamamoto, T.; Ikuhara, Y. *Appl. Phys. Lett.* **2009**, *95*, 191913.
(30) Findlay, S. D.; Shibata, N.; Sawada, H.; Okunishi, E.; Kondo, Y.; Ikuhara, Y. *Ultramicroscopy* **2010**, *110*, 903.
(31) Rusakov, D. A.; Abakumov, A. M.; Yamaura, K.; Belik, A. A.; Van Tendeloo, G.; Takayama-Muromachi, E. *Chem. Mater.* **2011**, *23*, 285.
(32) Karimi, S.; Reaney, I. M.; Levin, I.; Sterianou, I. *Appl. Phys. Lett.* **2009**, *94*, 112903.
(33) Levin, I.; Karimi, S.; Provenzano, V.; Dennis, C. L.; Wu, H.; Comyn, T. P.; Stevenson, T. J.; Smith, R. I.; Reaney, I. M. *Phys. Rev. B* **2010**, *81*, 020103.
(34) Karimi, S.; Reaney, I. M.; Han, Y.; Pokorny, J.; Sterianou, I. *J. Mater. Sci.* **2009**, *44*, 5102.
(35) Levin, I.; Tucker, M. G.; Wu, H.; Provenzano, V.; Dennis, C. L.; Karimi, S.; Comyn, T.; Stevenson, T.; Smith, R. I.; Reaney, I. M. *Chem. Mater.* **2011**, *23*, 2166.
(36) Fujishita, H.; Katano, S. *J. Phys. Soc. Jpn.* **1997**, *66*, 3484.
(37) Hewat, A. W. *Ferroelectrics* **1974**, *7*, 83.
(38) (a) Ghosez, Ph.; Cockayne, E.; Waghmare, U. V.; Rabe, K. M. *Phys. Rev. B* **1999**, *60*, 836. (b) Waghmare, U. V.; Rabe, K. M. *Ferroelectrics* **1997**, *194*, 135. (c) Ghita, M.; Fornari, M.; Singh, D. J.; Halilov, S. V. *Phys. Rev. B* **2005**, *72*, 054114.
(39) Cowley, R. A. *Phys. Rev.* **1964**, *134*, A981.
(40) Mishra, S. K.; Mittal, R.; Pomjakushin, V. Yu.; Chaplot, S. L. *Phys. Rev. B* **2011**, *83*, 134105.
(41) Tomeno, I.; Tsunoda, Y.; Oka, K. *Phys. Rev. B* **2009**, *80*, 104101.
(42) Claridge, J. B.; et al. *J. Am. Chem. Soc.* **2009**, *131*, 14000.
(43) Trolier-McKinstry, S.; Biegalski, M. D.; Wang, J.; Belik, A. A.; Takayama-Muromachi, E.; Levin, I. *J. Appl. Phys.* **2008**, *104*, 044102.
(44) Belik, A. A.; Yusa, H.; Hirao, N.; Ohishi, Y.; Takayama-Muromachi, E. *Chem. Mater.* **2009**, *21*, 3400.
(45) Guennou, M.; Bouvier, P.; Chen, G. S.; Dkhil, B.; Haumont, R.; Garbarino, G.; Kreisel, J. Multiple high-pressure phase transitions in $BiFeO_3$. 2011, arXiv:1108.0704. arXiv.org e-Print archive. http://arxiv.org/abs/1108.0704. Submitted on 02 August, 2011.